ChemSusChem

Research Article
doi.org/10.1002/cssc.202200231

Chemistry Europe
European Chemical Societies Publishing

www.chemsuschem.org

Atomically Dispersed Cu Sites on Dual-Mesoporous N-Doped Carbon for Efficient Ammonia Electrosynthesis from Nitrate

Mengqiu Xu[+],[a] Qifan Xie[+],[b] Delong Duan[+],[c] Ye Zhang,[a] Yuhu Zhou,[a] Haiqiao Zhou,[a] Xiaoyu Li,[a] Yao Wang,[b] Peng Gao,*[a] and Wei Ye*[a]

The industrial Haber-Bosch process for ammonia synthesis is extremely important in modern society. However, it is energy intensive and leads to severe pollution, which has motivated eco-friendly NH_3 synthesis research. Electroreduction of contaminant nitrate ions back to NH_3 is an effective complement but is still limited by low NH_3 yields and nitrate-to-NH_3 selectivities. In this study, the electrochemical nitrate reduction reaction (NTRR) is carried out over a single-atom Cu catalyst. Atomically dispersed Cu sites anchored on dual-mesoporous N-doped carbon framework display excellent NTRR performance with NH_3 production rate of 13.8 $mol_{NH_3}\ g_{cat}^{-1}\ h^{-1}$ and NO_3^--to-NH_3 faradaic efficiency (FE) of 95.5% at −1.0 V. Cu–N–C catalyst can sustain continuous 120 h NTRR test in the simulated NH_3 synthesis scenarios with large current density (about 200 $mA\,cm^{-2}$) and amplified volume of NO_3^- solution (9 times). Theoretical calculations reveal that atomically dispersed Cu_1–N_4 sites reduce the energy barrier of potential-determining step in NTRR and promote the decomposition of primary intermediate in NO_3^--to-N_2 process. These findings provide a guideline for the rational design of highly active, selective and durable electrocatalysts for the NTRR.

Introduction

Chemical reduction of N_2 to produce NH_3 plays a central role in the world, as NH_3 is an important chemical feedstock for the manufacture of nitrogenous fertilizers, N-containing chemicals, spices and pharmaceuticals.[1] Moreover, NH_3 is also regarded as a potential carbon free hydrogen storage carrier.[2] The wide usage of fertilizer has greatly promoted the rapid development of agriculture which leads to the booming development of world population. Currently, industrial NH_3 synthesis, i.e., Haber–Bosch process, is carried out employing iron catalyst to catalyze N_2 and H_2 into NH_3 at high temperature (400–500 °C) and high pressure (20–30 MPa).[3,4] Because of harsh synthetic conditions as well as huge annual production makes NH_3 synthesis to be energy intensive which consumes about 1–2% global annual energy supply.[5] Undeniably, the extensive usage of fossil fuels in NH_3 synthesis leads to amount of CO_2 release and upsets the carbon balance in the atmosphere.[6]

Nitrates ions (NO_3^-), as one kind of environmental pollutants, are widely existed in water bodies.[7] Generally, nitrates in the environment mainly come from chemical fertilizers, industrial wastewater, liquid nuclear wastes, and livestock excrements.[8,9] To eliminate nitrates in the industrial wastewater, NO_3^- is usually reduced to useless N_2.[10,11] Electrochemical NTRR back to NH_3 not only can eliminate nitrates contamination, but also acquire useful chemical (NH_3), which is considered as a powerful complement to Haber-Bosch process for NH_3 synthesis.[12] Currently, some progresses have been made based on metal based catalysts in which NO_3^--to-NH_3 FE exceeds 90%.[13] However, NTRR to NH_3 is a multi-step coupling process involving eight electrons and nine protons, suggesting that by-products are inevitable.[14] Apart from principle product (NH_3), NO_2^-, N_2 as well as the competing evolved hydrogen always lower the overall NH_3 FE, especially at large current density (> 100 $mA\,cm^{-2}$).[15,16] Theoretically, NO_3^--to-N_2 is usually occurred on adjacent two metal atoms to facilitate N–N coupling. Reducing active particle size to atomic dispersion can inhibit the formation of N_2 to boost NH_3 FE.[12a,17] Beyond that, the mass transfer kinetics of ionic species in NTRR is another parameter to determine the optimal reduction current density. Although the mesoporous carbon matrix carrier for single-atom catalyst derived from MOF usually provides large specific surface area. NO_3^- can still hardly reach the inside active sites due to the large particle size and small pore structure of the carrier which limit the optimal current density.[18] Therefore, the optimal partial NH_3 current density can be further improved by tuning single-atom catalyst and porous structure engineering of the carrier.

[a] M. Xu,[+] Y. Zhang, Y. Zhou, H. Zhou, X. Li, Prof. P. Gao, Dr. W. Ye
College of Material, Chemistry and Chemical Engineering
Key Laboratory of Organosilicon Chemistry and Material Technology
Ministry of Education, Hangzhou Normal University
Hangzhou, Zhejiang 311121 (P. R. China)
E-mail: gaopeng@hznu.edu.cn
yewei@hznu.edu.cn
[b] Q. Xie,[+] Dr. Y. Wang
College of Materials Science and Engineering
Zhejiang University of Technology, Hangzhou, Zhejiang 310014 (P. R. China)
[c] D. Duan[+]
School of Chemistry and Materials Science
University of Science and Technology of China, Hefei, Anhui 230026 (P. R. China)
[+] These authors contributed equally to this work.

Supporting information for this article is available on the WWW under https://doi.org/10.1002/cssc.202200231

Herein, inspired by theoretical screening of active components and excellent catalytic performance of Cu in NTRR, Cu single-atom catalyst anchored on dual-mesoporous N-doped carbon framework catalyst is developed for NTRR.[19] Cu–N–C delivers an optimal NH_3 production rate of 13.8 mol_{NH_3} g_{cat}^{-1} h^{-1} and NH_3 FE of 95.5% with a current density of 180 mA cm^{-2} at −1.0 V *versus* reversible hydrogen electrode (RHE). Specifically, atomically dispersed Cu sites show a much-enhanced NH_3 production rate compared to that of Cu NPs/N–C, it is about 125.5 times higher than that of counterpart Cu NPs/N–C when normalized to the active Cu mass. Theoretical calculations reveal that atomically dispersed Cu sites lower the energy barrier of the potential-determining step in NO_3^--to-NH_3 and inhibit the formation of N–N coupling intermediates to improve NH_3 FE.

Results and Discussion

Atomically dispersed Cu sites on dual-mesoporous N-doped carbon matrix are synthesized by a two-step method. As illustrated in Figure 1a, cupric(II) acetylacetonate ($Cu(acac)_2$) is encapsulated in situ in the voids of zeolitic imidazolate framework (ZIF-8, denoted as $Cu(acac)_2$@ZIF-8). After a subsequent pyrolysis treatment at 900 °C, $Cu(acac)_2$ in the cavity of ZIF-8 is converted to atomically dispersed Cu sites anchored on N-doped carbon matrix. Owing to low boiling point of metal Zn, Zn^{2+} which is acted as metal linker in ZIF-8 is evaporated to leave N-doped carbon framework.[20] As determined by inductively coupled plasma mass spectrometry (ICP-MS), Cu content in the final sample is 0.30 wt. %. Powder X-ray diffraction patter (XRD; see the Supporting Information, Figure S1) indicates that the sample exhibits no obvious diffraction peaks, suggesting no metallic Cu nanoparticle is formed after high-temperature pyrolysis.

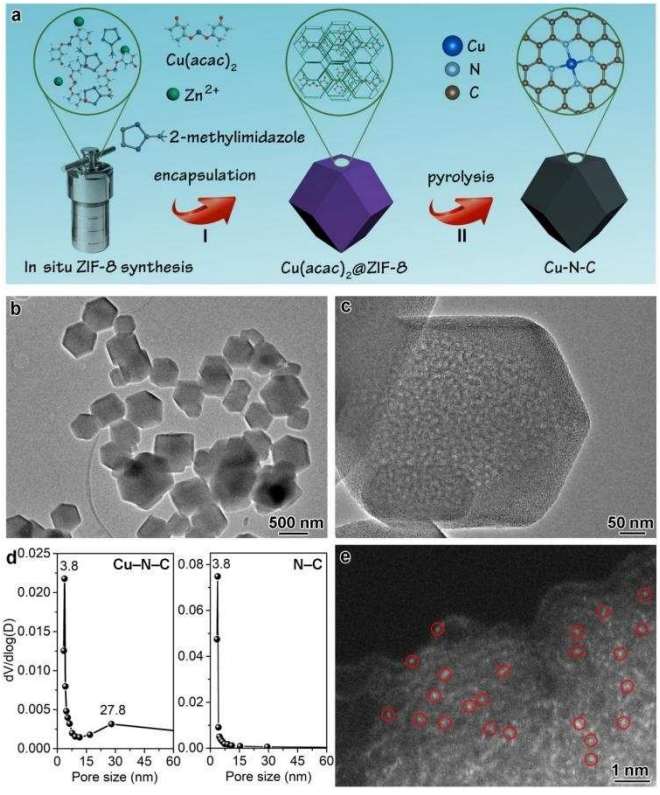

Figure 1. (a) Schematic depiction of the two-step synthesis of Cu–N–C: Step I: in situ encapsulation of $Cu(acac)_2$ in the cavity of ZIF-8 to form $Cu(acac)_2$@ZIF-8; step II: high-temperature pyrolysis to obtain atomically dispersed Cu anchored on dual-mesoporous N-doped carbon. (b,c) TEM images. (d) Comparison of pore size distributions for Cu–N–C and N–C samples. (e) HAADF-STEM image of Cu–N–C sample.

Transmission electron microscopy (TEM; Figure 1b) and scanning electron microscopy (SEM; Figure S2a) images reveal that the sample is polyhedron structure with size about 300–500 nm. The enlarged TEM images of a single nanoparticle (Figures 1c and S3) reveal large mesoporous structure in the inside of particle with a small mesoporous outermost layer. The diameter of inner pore size is about 20 nm (Figure S3b). To further characterize the pore structure, N_2 adsorption and desorption test is performed (Figure S4). Cu–N–C sample exhibits a large Brunauer–Emmett–Teller (BET) surface area of 926.9 m^2 g^{-1}. Pore size distributions (Figure 1d) indicate two kinds of mesoporous structures in Cu–N–C with pore sizes are mainly located at 3.8 and 27.8 nm, respectively. The large mesopores (27.8 nm) are located in the inside of the polyhedron and the small mesopores (3.8 nm) are exhibited in the outermost layer, respectively, consistent with TEM result. This kind of novel dual-mesoporous structure is totally different from that of ZIF-8 derived porous carbon with transition metals, such as Fe, Ni, Co, Mo, Ru, or Ir.[21] In contrast with the pyrolysis of ZIF-8 to produce N-doped carbon (Figure S5), the formation of large pore inside the polyhedron should be the result of Cu catalyzed high-temperature carbonization process.[22,23] This conclusion can be verified by Raman spectroscopy measurement in which Cu–N–C displays lower I_D/I_G ratio (Figure S6), suggesting higher degree of graphitization for Cu–N–C sample than that of N–C.[24] To further reveal the exact atomic Cu species, atomic resolution aberration-corrected high-angle annular dark-field scanning TEM (HAADF-STEM) is used to characterize the Cu–N–C sample. Atomically dispersed Cu sites are randomly distributed on N-doped carbon matrix (highlighted by red circles in Figures 1e and S7). Energy-dispersive X-ray spectroscopy (EDS) elemental mapping results (Figure S8) indicate that Cu, N, and C are uniformly distributed all over the sample.

To further reveal the exact fine structure of atomically dispersed Cu sites, Cu–N–C sample is characterized by synchrotron radiation-based X-ray absorption fine structure (XAFS) spectroscopy. Before that, X-ray photoelectron spectroscopy (XPS) characterization is performed which confirms the existence of Cu, N and C (Figure S9), consistent with EDS mapping result. High resolution of N1s spectrum (Figure 2a) is divided into three peaks located at 398.4, 400.4 and 403.2 eV, which can be assigned to pyridine N, pyrrolic N and graphitic N, respectively.[20,25] Cu2p spectrum (Figure S9b) is deconvoluted into two peaks located at 933.1 and 954.3 eV, which can be attributed to $2p_{3/2}$ and $2p_{1/2}$ of Cu^{δ}, respectively. The binding

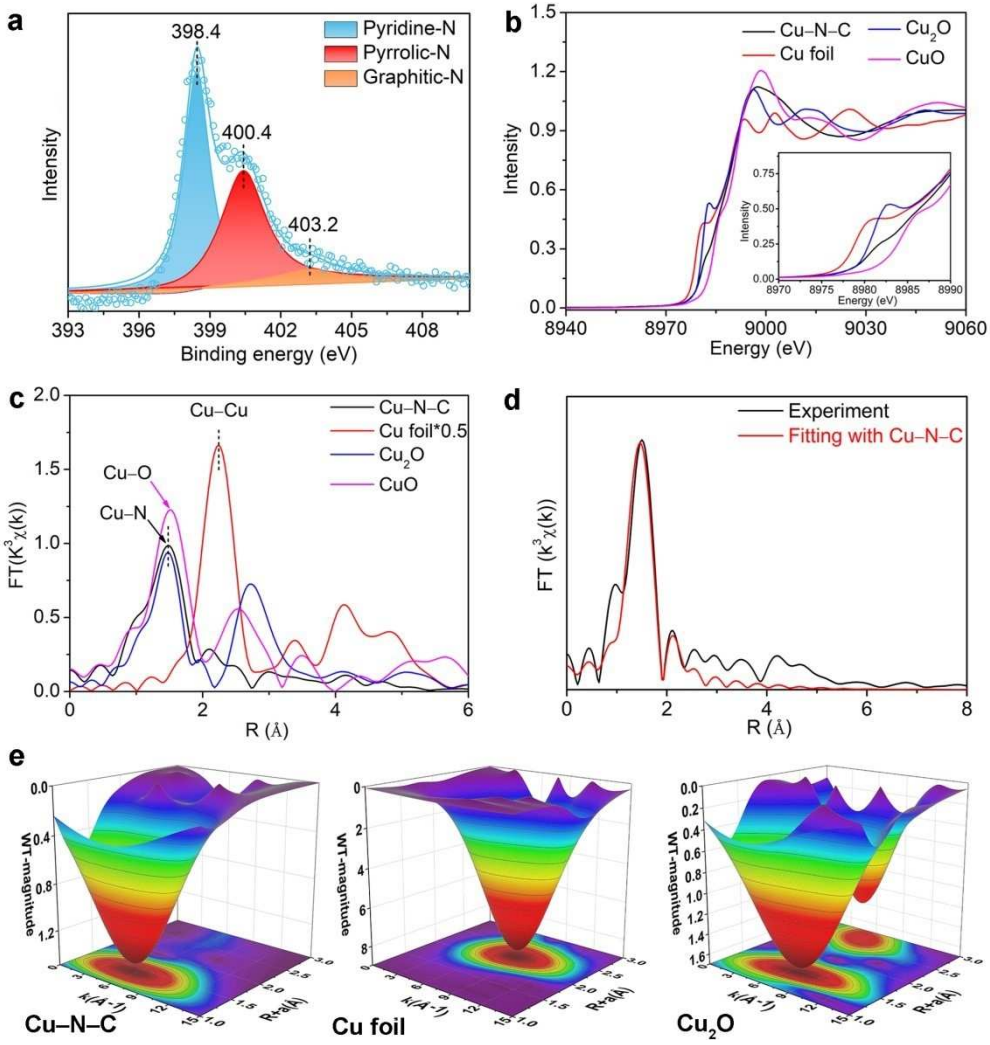

Figure 2. (a) N1s spectrum of Cu–N–C. (b) normalized Cu K-edge XANES spectra of Cu–N–C in reference to Cu foil, Cu_2O, and CuO. (c) k^3-weighted Fourier-transform Cu K-edge EXAFS spectra. (d) k^3-weighted Fourier-transform experimental Cu K-edge EXAFS spectrum (red line) and fitting curve (black line) of Cu–N–C. (e) Wavelet transforms for the k^3-weighted Cu K-edge EXAFS signals.

energy of $Cu2p_{3/2}$ is located between Cu_2O and CuO, suggesting $1 < \delta < 2$.[26] Figure 2b shows Cu K-edge X-ray absorption near-edge structure (XANES) spectra of Cu–N–C in reference to Cu_2O, CuO and Cu foil. A shoulder between 8980 and 8985 eV for Cu–N–C is located between Cu_2O and CuO, further verifying the oxidation state of Cu^{δ} is located between $+1$ and $+2$.[27] Owing to electrostatic interaction, Cu^{δ} facilitates the adsorption of NO_3^- which boost NTRR performance (Figure S10).[28]

To further decode the local structure of Cu atoms, we obtain the corresponding Cu extended XAFS (EXAFS) spectra through a Fourier transformation of K-edge spectra (Figure 2c and Table 1). In contrast with Cu foil, Cu–Cu bond is absent in Cu–N–C sample indicating that atomically dispersed Cu is existed in the sample rather than Cu cluster. In addition to Cu–Cu bond, Cu–N bond is also resolved in the first shell, suggesting that atomically dispersed Cu is anchored on N-doped carbon framework by forming Cu–N bond. The coordination numbers (CNs) of Cu–C/N in Cu–N–C sample is 3.97, suggesting that each Cu atom is bonded to four N atoms. The coordination structure of Cu_1–N_4–C_x is further analyzed by fitting the k^3-weighted Fourier transform EXAFS spectra (Figure 2d). It turns out that the fitting spectrum is almost overlapped with the experiment curve in the first shell, confirming the precise Cu_1–N_4–C_x coordination structure. Then, wavelet transforms (WT) analysis of the Cu K-edge EXAFS oscillations for Cu_1–N_4–C_x is performed in reference to Cu_2O

Table 1. Fitting results of Cu K-edge EXAFS data for Cu–N–C in reference to Cu_2O and Cu foil.[a]

Sample	Scattering	CN	R [Å]	σ^2 [10^{-3} Å^2]
Cu foil	Cu–Cu	12 (fixed)	2.54 ± 0.01	8.85
Cu_2O	Cu–O	2 (fixed)	1.84 ± 0.01	2.88
	Cu–Cu	12 (fixed)	3.05 ± 0.03	26.17
Cu–N–C	Cu–C/N	3.97 ± 0.41	1.92 ± 0.08	6.93

[a] CN = coordination numbers; R = bond length; σ^2 = Debye-Waller factor.

and Cu foil, respectively. As shown in Figure 2e, Cu–N–C sample exhibits a single intensity maximum at ~7.3 $Å^{-1}$ in three-dimensional WT contour plot, which can be assigned to Cu–N contribution in the first shell. In contrast with Cu foil, Cu–Cu signal is not observed in Cu–N–C sample, further confirming atomically dispersed Cu feature in Cu–N–C sample.

In view of Cu single-atom dispersion and dual-mesoporous N-doped carbon framework, electrochemical NTRR performance is assessed. All NTRR test is carried out in H-type cell in which the mixture of 1 M KNO_3 and 1 M KOH is used as electrolyte. Linear sweep voltammetry (LSV; Figure 3a) curve for Cu–N–C shows remarkably strengthened reduction current density compared with that of N–C sample, suggesting that atomically dispersed Cu sites can boost NTRR performance. After introducing SCN^- in the electrolyte to block Cu sites, LSV curve is almost overlapped with that of N–C sample, verifying that atomically dispersed Cu sites are indeed the active sites for NTRR.[27] NTRR is triggered by applying a given bias and the recorded *i–t* curves are shown in Figure S11. The produced NH_3 in the cathode chamber is quantified by colorimetric method of Nessler reagent and ^1H NMR (Figures S12 and S13). Figure 3b and 3c show the NH_3 production rate and the corresponding NH_3 FE for Cu–N–C in reference to N–C and Cu nanoparticles (Cu NPs, 20 wt.%) loaded on N-doped carbon (Figure S14), respectively. The NH_3 production rate is gradually enhanced as the potential moves to more negative region. The maximum NH_3 generation rate reaches 13.8 $mol_{NH_3}\ g_{cat}^{-1}\ h^{-1}$ for Cu–N–C sample at −1.0 V versus RHE.

In stark contrast, Cu NPs and N–C samples deliver the best NH_3 production rate of 7.3 and 2.4 $mol_{NH_3}\ g_{cat}^{-1}\ h^{-1}$ at −1.0 and

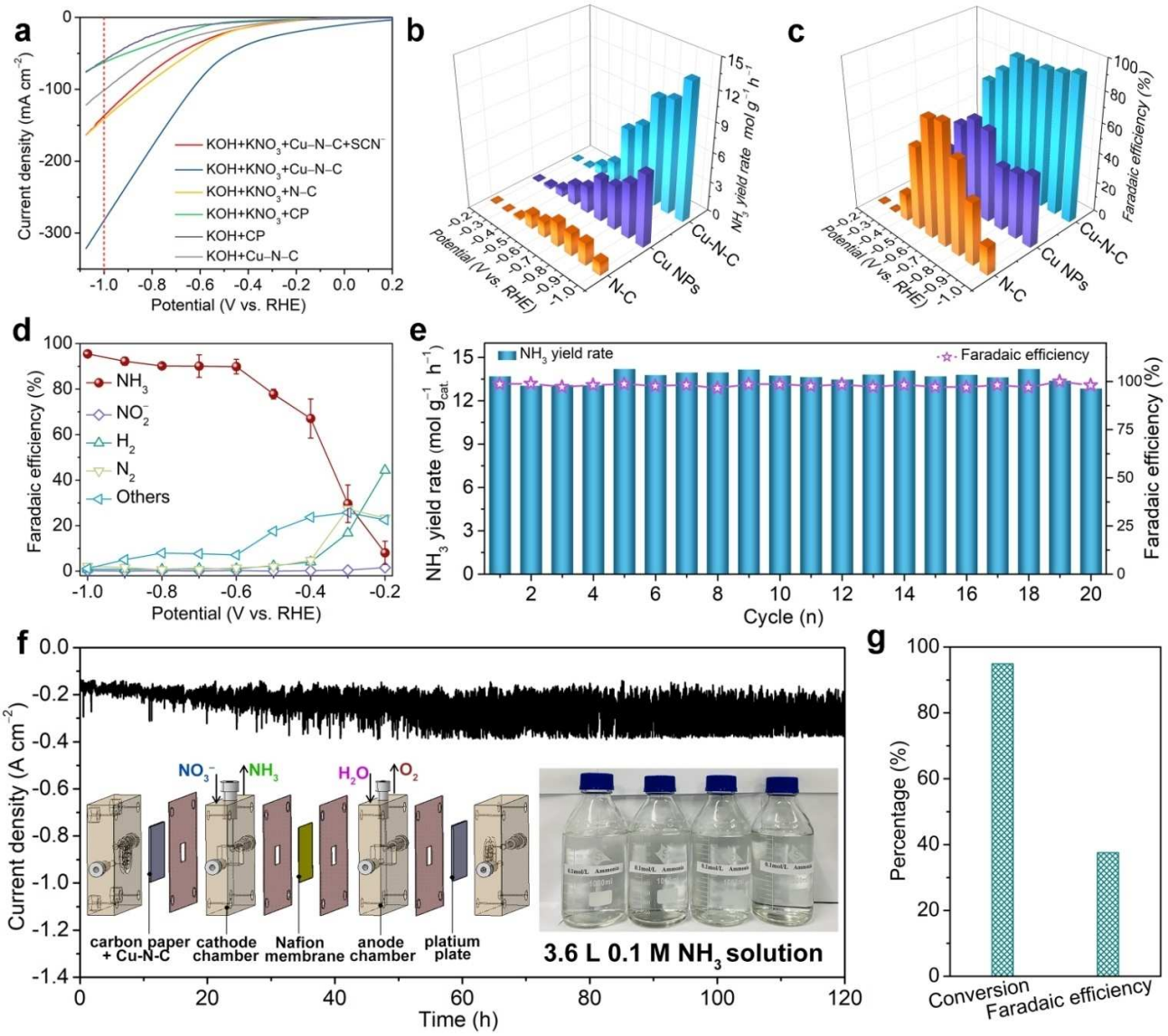

Figure 3. (a) LSV curves of Cu–N–C in the mixture of 1 M KOH and 1 M KNO_3. (b) NH_3 production rate and (c) the corresponding NO_3^--to-NH_3 FE for Cu–N–C in reference to Cu NPs and N–C, respectively. (d) Potential-dependent FEs of NH_3, NO_2^-, N_2 and H_2 for Cu–N–C. (e) Cycling stability test. Flow cell and its performance: (f) *i–t* curve and (g) conversion of NO_3^- and NH_3 FE. The insets in 3f show a schematic illustration of the flow cell for continuous production of NH_3 (left) and the obtained diluted 0.1 M NH_3 solution (right).

−0.7 V, respectively. NH_3 production rate for Cu–N–C is about 1.9 and 5.8 times higher than that of Cu NPs and N–C, respectively. Surprisingly, NH_3 production rate for Cu–N–C is 125.5 times higher than that of Cu NPs when normalized to active Cu mass (Figure S15), further confirming the excellent NTRR performance for single-atom Cu catalysts. Notably, as far as we know, this is the highest NH_3 production rate so far (Table S1). The huge NH_3 production rate improvement on Cu single-atom sites can be ascribed to the following two reasons: 1) atomically dispersed Cu sites and unique Cu_1–N_4 coordination structure. 2) Unique dual-mesoporous structure improves mass transfer kinetics and increases the electrochemical active area (Figures S16 and S17). As shown in Figure 3c, NO_3^--to-NH_3 FE for Cu–N–C also increases with decreasing potential and reaches 95.5% at −1.0 V, suggesting that electrons are almost used for NTRR at more negative potential. In contrast, optimal NO_3^--to-NH_3 FEs are only 63.2 and 80.2% for Cu NPs and N–C samples at −0.6 and −0.7 V, respectively. This result indicates that atomic dispersion of Cu sites on dual-mesoporous N–C plays a vital role in NTRR.

To further test whether the produced NH_3 is derived from the reduction of NO_3^-, a ^{15}N isotope labeling experiment was performed (Figure S18). The ^1H NMR spectrum recorded in $^{14}NO_3^-$ shows a triplet pattern with the coupling constant of $J_{N-H}=52$ Hz, which can be assigned to standard NH_4Cl.[29] When $^{15}NO_3^-$ is used as N resource, a doublet pattern with the coupling constant of $J_{N-H}=72$ Hz is detected, which is attributed to $^{15}NH_4^+$.[30] The possible byproducts in NTRR (NO_2^-, N_2 and H_2) are also quantified by colorimetric method of Griess reagent (Figure S19) and gas chromatography (GC, S20), respectively. As indicated in Figure 3d, H_2 FE for Cu–N–C is 44.4% at −0.2 V and then gradually declines to approaching zero at −0.5 V, suggesting the competing hydrogen evolution reaction (HER) is effectively suppressed on Cu_1–N_4 sites, especially at more negative potential (−0.5 to −1.0 V), which is extremely important in real application. Accordingly, NH_3 FE sharply increases to 90.0% at −0.6 V and then slowly increases to approaching 100% when further decreasing potential to −1.0 V. Similarly, FEs of N_2 and NO_2^- are extremely low between −0.4 and −1.0 V, indicating the excellent NH_3 selectivity for Cu–N–C sample. In stark contrast, N_2 FE for Cu NPs is dominated between −0.4 and −1.0 V, suggesting that metallic Cu cluster is in favor of the formation of N_2 (Figure S21).

To further inspect the role of Cu single-atom sites on NTRR, the relationship of NTRR performance with Cu loading is investigated. NH_3 production rate and FE show a linear relation with the dosage of $Cu(acac)_2$ (Figure S22). To reveal wide applicability for Cu–N–C sample in NTRR, we further assess NTRR performance in various concentrations of NO_3^- and pH of the electrolyte (Figures S23 and S24). It is found that NTRR can be carried out in the concentration range of 0.05 to 1.00 M of KNO_3 and in the pH range of 7 to 14. NH_3 production rate and NO_3^--to-NH_3 FE are positively correlated with the concentrations of NO_3^- and pH.

Apart from NTRR activity, durability is another important parameter. Figure 3e shows the durability test which turns out that Cu–N–C sample can sustain successive 20 cycles without obvious NH_3 production rate and faradaic efficiency decay. After 20 cycles test, dual-mesoporous Cu–N–C structure is well maintained, suggesting the excellent stability of catalyst (Figure S25). In view of the excellent NTRR activity and stability for Cu–N–C sample, we further simulate industrial NH_3 electrosynthesis scenarios in a flow cell. The volume of the cathode electrolyte is increased by 9 times to 360 mL (1 M KNO_3; Figure S26). Amazingly, Cu–N–C can sustain continuous 120 h NTRR catalysis and 94.8% of NO_3^- is converted to NH_3 with NH_3 FE of 37.5% in flow cell (Figure 3f,g). Finally, we obtain 3.6 L NH_3 solution (0.1 M). This excellent scale-up test result shows bright application prospect in real industrial catalysis with our Cu–N–C catalyst.

Upon assessing NTRR performance of Cu–N–C, density functional theory (DFT) calculation is employed to further understand the mechanism of Cu_1–N_4 sites to promote NTRR. NTRR is a proton coupling process of eight electrons and nine protons where five possible pathways are involved in NTRR (Figure S27).[24] Figure 4a and 4b show the minimum energy pathway and the corresponding adsorption configurations of the intermediates in NTRR process. It is found that NTRR is carried out on Cu_1–N_4 sites adopting pathway 2 where the potential-determining step is *NO→*HNO with an energy barrier of 0.38 eV. As a byproduct, NO_3^--to-N_2 is proceeded by a coupling process of *NO→*N_2O_3 and then *N_2O_3→N_2O_2OH (−0.09 eV). Although, the two above steps are exothermic processes which seems that N_2 is preferred to obtain on Cu_1–N_4 sites. In fact, the intermediate of *N_2O_3 is more likely to decompose into *NO and *HNO_2 with a larger energy decline (−0.31 eV). Then, the obtained *NO and *HNO_2 intermediates are further converted to NH_3 through pathway 2, suggesting that N_2 is prohibitive on Cu_1–N_4 sites. The energy diagram well explains the approaching 100% NH_3 FE in NTRR for Cu–N–C catalyst. Similarly, NTRR on Cu cluster loaded on N-doped carbon framework is also carried out which also involves five possible pathways (Figures S28 and S29). Figure 4c shows the minimum energy pathway on Cu cluster (pathway 3). The potential-determining step is *NH_2→*NH_3 with $\triangle G$ of 0.57 eV. Obviously, the energy barrier of potential-determining step for Cu cluster is larger than that of Cu_1–N_4 sites, which well illustrates better NTRR activity on Cu–N–C sample than Cu NPs. For the conversion of NO_3^--to-N_2, the energy is all declining from the processes of *NO→*N_2 + *OH (Figure S30). Although, the following two steps of *N_2 + *OH→N_2 + *OH→* + N_2 are endothermic reactions with energy barriers of 0.56 and 0.11 eV, respectively. The energy barrier of 0.56 eV is comparable with that of potential-determining step in NO_3^--to-N_2. Besides, the huge energy release for the previous step of *N_2O→*N_2 + *OH will partially compensate the following two steps. These two facts indicate that NO_3^--to-N_2 on Cu cluster/N–C is energetically possible which well explains the byproduct of N_2 is obtained for Cu cluster/N–C sample.

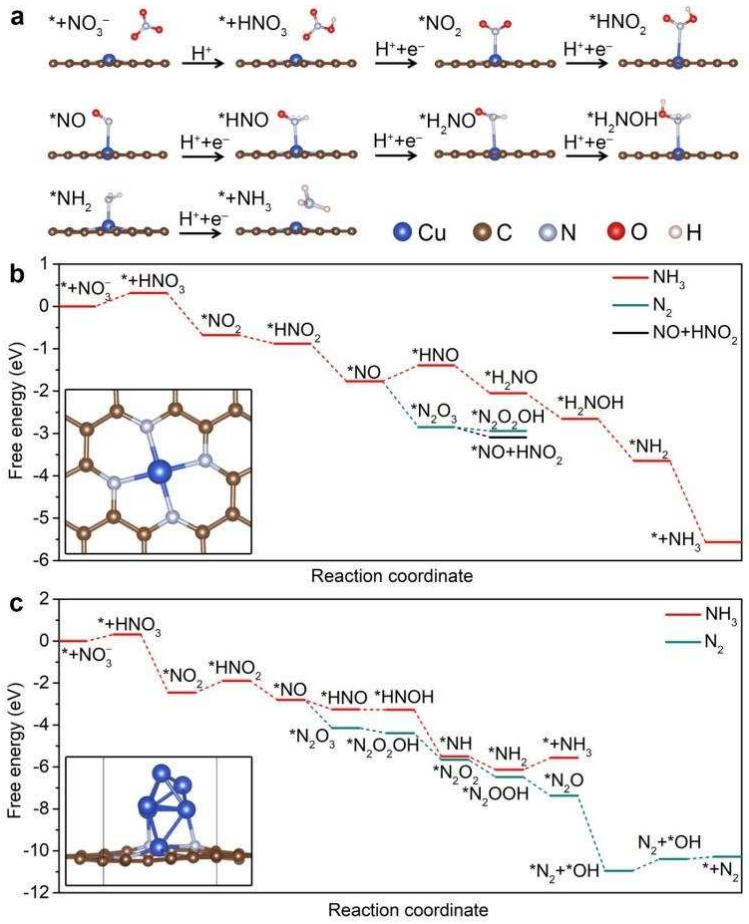

Figure 4. (a) The minimum energy pathway that results in NH_3 as the main product. Free energy diagram showing the minimum energy pathway at $U = 0.0$ V vs. RHE: (b) Cu–N–C catalyst and (c) Cu cluster.

Conclusion

In summary, atomically dispersed Cu anchored on dual-mesoporous N-doped carbon framework was prepared through in situ encapsulation of the Cu precursor in ZIF-8 followed by high-temperature pyrolysis. The dual-mesoporous carbon framework facilitated mass transfer of NO_3^- to reach the inner active site and improved the optimal reduction current density. Atomically dispersed Cu_1–N_4 sites lowered the energy barrier of the potential-determining step in NTRR and promoted decomposition of the primary intermediate in the conversion of NO_3^- into N_2. Benefiting from the dual-mesoporous structure and atomically dispersed Cu sites, Cu–N–C gave a high ammonia production rate of 13.8 mol_{NH_3} g_{cat}^{-1} h^{-1} with NH_3 FE of 95.5% at −1.0 V. More importantly, Cu–N–C shows high potential for application as a catalyst in real NTRR with a large current density (200 mA cm^{-1}) and durability (120 h). This work opens up new opportunities for the preparation and application of highly efficient and stable Cu-based single-atom NTRR catalysts.

Experimental Section

Materials

Cupric(II) acetylacetonate ($C_{10}H_{14}CuO_4$, A.R.), 2-Methylimidazole ($C_4H_6N_2$, A.R.), zinc nitrate hexahydrate ($(Zn(NO_3)\cdot 6H_2O$, A.R.), methanol (CH_4O, A.R.), ammonium chloride (NH_4Cl, A.R.), sodium nitrite ($NaNO_2$, A.R.), ethanol (EtOH, A.R.), ^{15}N-labeled potassium nitrate ($K^{15}NO_3$, ≥ 99.5%), potassium nitrate (KNO_3, A.R.), potassium hydroxide (KOH, A.R.), ultra-high purity Ar (99.999%), Nessler reagent, Griess reagent and Nafion (5 wt.%) were purchased from Sinopharm Chemical Reagent Co. Ltd. (Shanghai, China). All chemicals were used without further purification. All aqueous solutions were prepared using deionized (DI) water with a resistivity of 18.25 MΩ cm^{-1}.

Synthesis of $Cu(acac)_2$@ZIF-8

2-Methylimidazole (1314 mg) was dissolved in methanol (15 mL) to obtain solution A. Then, zinc nitrate hexahydrate ($Zn(NO_3)\cdot 6H_2O$, 1190 mg) and cupric(II) acetylacetonate ($Cu(acac)_2$, 1190 mg) were dissolved in another methanol (30 mL) to obtain solution B. After that, solution B was added into solution A, ultrasound 5 min and leave it along for another 1 h. At last, the mixture was transferred and sealed in an autoclave with a Teflon liner, and was heated at 120 °C for 4 h. The product was collected with centrifugation and

washed with ethanol five times, dried at 60 °C under vacuum condition for 24 h. The protocol for the synthesis of ZIF-8 was similar with $Cu(acac)_2$@ZIF-8 without $Cu(acac)_2$.

Conversion of $Cu(acac)_2$@ZIF-8 to Cu–N–C

The powder of $Cu(acac)_2$@ZIF-8 was crushed, transferred into a quartz boat, and placed in the middle of tube furnace. The sample was heated to 900 °C with a heating rate of 5 °C min^{-1}, kept at 900 °C for 3 h under argon gas flow, and then naturally cooled to room temperature.

Synthesis of Cu nanoparticle loaded on N–C

N–C powder (100 mg) was ultrasonic dispersed in the mixture of water (10 mL) and $CuCl_2 \cdot 2H_2O$ (53.2 mg). The mixture was quickly frozen in liquid nitrogen and freeze-drying for 2 days. Finally, the sample was calcined in Ar atmosphere for 3 h.

XAFS characterization

Cu K-edge XAFS measurements were performed at the beamline 14 W1 in Shanghai Synchrotron Radiation Facility (SSRF), China. The X-ray was monochromatized by a double-crystal Si(111) monochromator. The storage ring of SSRF was operated at 3.5 GeV with the current of 300 mA. The acquired extended XAFS (EXAFS) data were processed according to the standard procedures using the WinXAS3.1 program.[31] Theoretical amplitudes and phase-shift functions were calculated with the FEFF8.2 code.[32]

Electrochemical nitrate reduction test

2 mg Cu–N–C sample was ultrasonically dispersed in a mixture of water (0.7 mL), isopropanol (0.25 mL) and Nafion (50 μL, 5 wt.%) to form the catalyst ink. Then, the catalyst slurry (50 μL) was dropped onto 1×1 cm^2 carbon paper (catalyst loading amount: 0.1 mg cm^{-2}). Then, it was dried naturally which was then used as working electrode combined with Ag/AgCl as reference electrode and Pt mesh as counter electrode, respectively. All nitrate reduction tests were performed using a three-electrode system in a H-type cell in which cathode chamber and anode chamber was separated by commercial F117 membrane. The mixture of 1 M KOH + 1 M KNO_3 solution was used as the electrolyte. The electrolyte was bubbled by continuous high purity Ar for 30 min and then nitrate reduction reaction was triggered by applying a fixed potential from −0.2 to −1.0 V (V vs. RHE) for 1 h. The produced NH_3 in cathode chamber was quantified by colorimetric method and ^1H NMR spectra. The by-products of NO_2^-, H_2 and N_2 was determined and quantified by colorimetric method and gas chromatography, respectively.

Theoretical calculations

All calculations were based on density functional theory (DFT) and implemented in the Vienna Ab initio Simulation Package (VASP).[33,34] The plane-wave pseudopotentials with Perdew-Burke-Ernzerhof (PBE) exchange-correlation functional were used in the calculations.[35] The cutoff energy was 400 eV for the plane-wave expansion. A single gamma *k*-point was set for all calculations. The DFT-D3 method was employed to correct the van der Waals (vdW) interactions.[36] To avoid artificial interactions between two layers, the vacuum spacing was set as 20 Å. For all calculations, the convergence criterions of energy and force were set to be 10^{-4} eV and 0.02 eV $Å^{-1}$, respectively.

According to the method presented by Nørskov and co-workers, the Gibbs free energy change was estimated under zero potential ($U = 0$) by using Equation (1):[37]

$$\Delta G = \Delta E_{DFT} + \Delta ZPE - T\Delta S \quad (1)$$

where E_{DFT} is the energy obtained from DFT calculations, ZPE is the zero-point energy, and T and S denote the temperature and entropy, respectively. There are five possible pathways involved in NTRR, which are listed in the Supporting Information.

Acknowledgements

This work was financially supported in part by the Natural Science Foundation of China (51902077), Zhejiang Provincial Natural Science Foundation (LQ19B010001), Zhejiang Province "Ten Thousand People Plan" and general items of Zhejiang Provincial Department of Education (Y201840068).

Conflict of Interest

The authors declare no conflict of interest.

Data Availability Statement

The data that support the findings of this study are available from the corresponding author upon reasonable request.

Keywords: ammonia · copper · electrocatalysis · reduction · single-atom catalysts

[1] a) V. Rosca, M. Duca, M. T. Groot, M. T. M. Koper, *Chem. Rev.* **2009**, *109*, 2209–2244; b) D. R. MacFarlane, P. V. Cherepanov, J. Choi, B. H. R. Suryanto, R. Y. Hodgetts, J. M. Bakker, F. M. F. Vallana, A. N. Simonov, *Joule* **2020**, *4*, 1186–1205; c) A. J. Martın, T. Shinagawa, J. Pe'rez-Ramırez, *Chem* **2019**, *5*, 263–283; d) T. Ye, S. Park, Y. Lu, J. Li, M. Sasase, M. Kitano, T. Tada, H. Hosono, *Nature* **2020**, *583*, 391–395; e) Y. Zhang, J. Zhao, D. Yang, B. Wang, Y. Zhou, J. Wang, H. Chen, T. Mei, S. Ye, J. Qu, *Nat. Catal.* **2021**, *4*, 989–990.
[2] D. D. Papadias, J. Peng, R. K. Ahluwalia, *Int. J. Hydrogen Energy* **2021**, *46*, 24169–24189.
[3] A. Barafiski, A. Kotarba, J. M. Lagan, A. Pattek-Janczyk, E. Pyrczak, A. Reizer, *Appl. Catal. A* **1994**, *112*, 13–36.
[4] X. Zhu, S. Mou, Q. Peng, Q. Liu, Y. Luo, G. Chen, S. Gao, X. Sun, *J. Mater. Chem. A* **2020**, *8*, 1545–1556.
[5] B. Yang, W. Ding, H. Zhang, S. Zhang, *Energy Environ. Sci.* **2021**, *14*, 672–687.
[6] C. Tang, S. Z. Qiao, *Chem. Soc. Rev.* **2019**, *48*, 3166–3180.
[7] M. H. Ward, R. R. Jones, J. D. Brender, T. M. Kok, P. J. Weyer, B. T. Nolan, C. M. Villanueva, S. G. Breda, *Int. J. Environ. Res. Public Health* **2018**, *15*, 1557.
[8] G. Chen, Y. Yuan, H. Jiang, S. Ren, L. Ding, L. Ma, T. Wu, J. Lu, H. Wang, *Nat. Energy* **2020**, *5*, 605–613.
[9] X. Zhang, Y. Wang, C. Liu, Y. Yu, S. Lu, B. Zhang, *Chem. Eng. J.* **2021**, *403*, 26269.
[10] T. Zhu, Q. Chen, P. Liao, W. Duan, S. Liang, Z. Yan, C. Feng, *Small* **2020**, *16*, 2004526.
[11] H. Shi, C. Li, L. Wang, W. Wang, X. Meng, *J. Hazard. Mater.* **2022**, *424*, 127711.

[12] a) P. Li, Z. Jin, Z. Fang, G. Yu, *Energy Environ. Sci.* **2021**, *14*, 3522–3531; b) Y. Wang, C. Wang, M. Li, Y. Yu, B. Zhang, *Chem. Soc. Rev.* **2021**, *50*, 6720–6733; c) J. Wang, T. Feng, J. Chen, V. Ramalingam, Z. Li, D. M. Kabtamu, J. He, X. Fang, *Nano Energy* **2021**, *86*, 106088.
[13] a) Y. Wang, W. Zhou, R. Jia, Y. Yu, B. Zhang, *Angew. Chem. Int. Ed.* **2020**, *59*, 5350–5354; *Angew. Chem.* **2020**, *132*, 5388–5392; b) Y. Wang, A. Xu, Z. Wang, L. Huang, J. Li, F. Li, J. Wicks, M. Luo, D. Nam, C. Tan, Y. Ding, J. Wu, Y. Lum, C. Dinh, D. Sinton, G. Zheng, E. H. Sargent, *J. Am. Chem. Soc.* **2020**, *142*, 5702–5708; c) P. H. Langevelde, I. Katsounaros, M. T. M. Koper, *Joule* **2021**, *5*, 290–294.
[14] J. Li, G. Zhan, J. Yang, F. Quan, C. Mao, Y. Liu, B. Wang, F. Lei, L. Li, A. W. M. Chan, L. Xu, Y. Shi, Y. Du, W. Hao, P. K. Wong, J. Wang, S. Dou, L. Zhang, J. C. Yu, *J. Am. Chem. Soc.* **2020**, *142*, 7036–7046.
[15] M. Xu, F. Xu, K. Zhu, X. Xu, P. Deng, W. Wu, W. Ye, Z. Sun, P. Gao, *Comp. Commun.* **2022**, *29*, 101037.
[16] Q. Hu, Y. Qin, X. Wang, Z. Wang, X. Huang, H. Zheng, K. Gao, H. Yang, P. Zhang, M. Shao, C. He, *Energy Environ. Sci.* **2021**, *14*, 4989–4997.
[17] Z. Wu, M. Karamad, X. Yong, Q. Huang, D. A. Cullen, P. Zhu, C. Xia, Q. Xiao, M. Shakouri, F. Chen, J. Y. Kim, Y. Xia, K. Heck, Y. Hu, M. S. Wong, Q. Li, I. Gates, S. Siahrostami, H. Wang, *Nat. Commun.* **2021**, *12*, 2870.
[18] J. Liu, Z. Gong, C. Allen, W. Ge, H. Gong, J. Liao, J. Liu, K. Huang, M. Yan, R. Liu, G. He, J. Dong, G. Ye, H. Fei, *Chem Catal.* **2021**, *1*, 1291–1307.
[19] a) X. Zhao, X. Li, H. Zhang, X. Chen, J. Xu, J. Yang, H. Zhang, G. Hu, *J. Hazard. Mater.* **2022**, *424*, 127319; b) X. Zhao, X. Jia, Y. He, H. Zhang, X. Zhou, H. Zhang, S. Zhang, Y. Dong, X. Hu, A. V. Kuklin, G. V. Baryshnikov, H. Agren, G. Hu, *Appl. Mater. Res.* **2021**, *25*, 101206; c) X. Zhao, Z. Zhu, Y. He, H. Zhang, X. Zhou, W. Hu, M. Li, S. Zhang, Y. Dong, X. Hu, A. V. Kuklin, G. V. Baryshnikov, H. Ågren, T. Wågberg, G. Hu, *Chem. Eng. J.* **2022**, *433*, 133190; d) X. Zhao, G. Hu, F. Tan, S. Zhang, X. Wang, X. Hu, A. V. Kuklin, G. V. Baryshnikov, H. Ågren, X. Zhou, H. Zhang, *J. Mater. Chem. A* **2021**,*9*, 23675–23686.
[20] W. Ye, S. Chen, Y. Lin, L. Yang, S. Chen, X. Zheng, Z. Qi, C. Wang, R. Long, M. Chen, J. Zhu, P. Gao, L. Song, J. Jiang, Y. Xiong, *Chem* **2019**, *5*, 2865–2878.
[21] a) Y. Chen, S. Ji, Y. Wang, J. Dong, W. Chen, Z. Li, R. Shen, L. Zheng, Z. Zhuang, D. Wang, Y. Li, *Angew. Chem. Int. Ed.* **2017**, *56*, 6937–6941; *Angew. Chem.* **2017**, *129*, 7041–7045; b) P. Yin, T. Yao, Y. Wu, L. Zheng, Y. Lin, W. Liu, H. Ju, J. Zhu, X. Hong, Z. Deng, G. Zhou, S. Wei, Y. Li, *Angew. Chem. Int. Ed.* **2016**, *55*, 10800–10805; *Angew. Chem.* **2016**, *128*, 10958–10963; c) Z. Geng, Y. Liu, X. Kong, P. Li, K. Li, Z. Liu, J. Du, M. Shu, R. Si, J. Zeng, *Adv. Mater.* **2018**, *30*, 1803498; d) M. Xiao, J. Zhu, G. Li, N. Li, S. Li, Z. P. Cano, L. Ma, P. Cui, P. Xu, G. Jiang, H. Jin, S. Wang, T. Wu, J. Lu, A. Yu, D. Su, Z. Chen, *Angew. Chem. Int. Ed.* **2019**, *58*, 9640–9645; *Angew. Chem.* **2019**,*131*, 9742–9747; e) Y. Wang, G. Jia, X. Cui, X. Zhao, Q. Zhang, L. Gu, L. Zheng, L. Li, Q. Wu, D. J. Singh, D. Matsumura, T. Tsuji, Y. Cui, J. Zhao, W. Zheng, *Chem* **2021**, *7*, 436–449; f) C. Zhao, X. Dai, T. Yao, W. Chen, X. Wang, J. Wang, J. Yang, S. Wei, Y. Wu, Y. Li, *J. Am. Chem. Soc.* **2017**, *139*, 8078–8081.
[22] J. Raoof, S. R. Hosseini, R. Ojani, S. Mandegarzad, *Energy* **2015**, *90*, 1075–1081.
[23] K. Zhao, X. Nie, H. Wang, S. Chen, X. Quan, H. Yu, W. Choi, G. Zhang, B. Kim, J. G. Chen, *Nat. Commun.* **2020**, *11*, 2455.
[24] O. A. Maslova, M. R. Ammar, G. Guimbretiere, J. Rouzaud, P. Simon, *Phys. Rev. B* **2012**, *86*, 134205.
[25] M. K. Kuntumalla, M. Attrash, R. Akhvlediani, S. Michaelson, A. Hoffman, *Appl. Surf. Sci.* **2020**, *525*, 146562.
[26] G. Panzner, B. Egert, H. P. Schmidt, *Surf. Sci.* **1985**, *151*, 400–408.
[27] B. Lee, S. Park, M. Kim, A. K. Sinha, S. C. Lee, E. Jung, W. J. Chang, K. Lee, J. H. Kim, S. Cho, H. Kim, K. T. Nam, T. Hyeon, *Nat. Mater.* **2019**, *18*, 620–626.
[28] B. Mao, P. Sun, Y. Jiang, T. Meng, D. Guo, J. Qin, M. Cao, *Angew. Chem. Int. Ed.* **2020**, *59*, 15232–15237; *Angew. Chem.* **2020**,*132*, 15344–15349.
[29] J. Liu, M. S. Kelley, W. Wu, A. Banerjee, A. P. Douvalis, J. Wu, Y. Zhang, G. C. Schatz, M. G. Kanatzidis, *Proc. Natl. Acad. Sci. USA* **2016**, *113*, 5530.
[30] F. Xu, F. Wu, K. Zhu, Z. Fang, D. Jia, Y. Wang, G. Jia, J. Low, W. Ye, Z. Sun, P. Gao, *Appl. Catal. B* **2021**, *284*, 119689.
[31] T. Ressler, *J. Synchrotron Radiat.* **1998**, *5*, 118–122.
[32] A. L. Ankudinov, B. Ravel, J. J. Rehr, S. D. Conradson, *Phys. Rev. B* **1998**, *58*, 7565–7576.
[33] G. Kresse, J. Furthmüller, *Phys. Rev. B* **1996**, *54*, 11169.
[34] G. Kresse, D. Joubert, *Phys. Rev. B* **1999**, *59*, 1758.
[35] J. P. Perdew, K. Burke, M. Ernzerhof, *Phys. Rev. Lett.* **1996**, *77*, 3865.
[36] S. Grimme, J. Antony, S. Ehrlich, H. Krieg, *J. Chem. Phys.* **2010**, *132*, 154104.
[37] J. K. Nørskov, T. Bligaard, A. Logadottir, J. R. Kitchin, J. G. Chen, S. Pandelov, U. Stimming, *J. Electrochem. Soc.* **2005**, *152*, 23.

Manuscript received: January 31, 2022
Revised manuscript received: February 27, 2022
Accepted manuscript online: April 5, 2022
Version of record online: ■■, ■■■

RESEARCH ARTICLE

A site to behold: Atomically dispersed Cu_1–N_4 sites anchored on dual-mesoporous N-doped carbon framework are developed as a catalyst for ammonia electrosynthesis from nitrate. The carbon carrier improves the mass transfer kinetics. Cu_1–N_4 sites inhibit the conversion of NO_3^- into N_2 to improve ammonia selectivity. Cu–N–C delivers an NH_3 production rate of 13.8 $mol_{NH_3}\ g_{cat}^{-1}\ h^{-1}$ and a faradaic efficiency of 95.5 %.

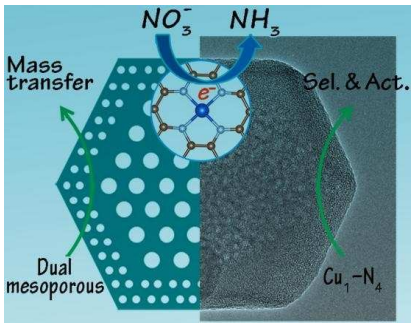

M. Xu, Q. Xie, D. Duan, Y. Zhang, Y. Zhou, H. Zhou, X. Li, Dr. Y. Wang, Prof. P. Gao, Dr. W. Ye**

1 – 9

Atomically Dispersed Cu Sites on Dual-Mesoporous N-Doped Carbon for Efficient Ammonia Electrosynthesis from Nitrate